Tunable magic wavelengths for trapping with focused Laguerre-Gaussian beams

Anal Bhowmik,[1,*] Narendra Nath Dutta,[2,†] and Sonjoy Majumder[1,‡]
[1]*Department of Physics, Indian Institute of Technology Kharagpur, Kharagpur-721302, India*
[2]*Department of Chemistry and Biochemistry, Auburn University, Alabama 36849, USA*

(Received 30 November 2017; published 21 February 2018)

We present in this paper a theory of dynamic polarizability for an atomic state due to an external field of nonparaxial Laguerre-Gaussian (LG) beam using the sum-over-states technique. A highly correlated relativistic coupled-cluster theory is used to evaluate the most important and correlation-sensitive parts of the sum. The theory is applied on Sr^+ to determine the magic wavelengths for $5s_{1/2} \rightarrow 4d_{3/2}, 4d_{5/2}$ transitions. Results show the variation of magic wavelengths with the choice of orbital and spin angular momenta of the incident LG beam. Also, the tunability of the magic wavelengths is studied by using the focusing angle of the LG beam and its efficiency in the near-infrared region is observed. Evaluations of the wide spectrum of magic wavelengths from infrared to ultraviolet have substantial importance to experimentalists for carrying out high-precision measurements in fundamental physics. These magic wavelengths can be used to confine the atom or ion at the dark central node or at the high-intensity ring of the LG beam.

DOI: 10.1103/PhysRevA.97.022511

I. INTRODUCTION

Mechanisms of cooling and trapping of atoms or ions using laser beams have been widely employed in high-precision spectroscopic measurements. To minimize the various systematics in the measurements of any spectroscopic properties [1,2], experimentalists need to trap the atoms at particular wavelengths of the external laser field where the differential ac Stark shift of an atomic transition effectively vanishes. These special wavelengths are named "magic wavelengths" and are used as to perform clock frequency measurements [3], optical frequency standards [4], etc. Another significant application of magic wavelengths is in quantum computation and communication schemes when the neutral atoms are trapped inside high-Q cavities at magic wavelengths in the strong-coupling regime [5].

Alkali-metal atoms are favorable candidates for performing experiments using laser cooling and trapping techniques. This is mainly because the low-lying transitions for these atoms are easily accessible by the available laser sources. Stellmer *et al.* [6] produced Bose-Einstein condensation of ^{88}Sr by using evaporative cooling and an optical dipole trap. A detailed study of sub-Doppler cooling of ^{87}Sr in a magneto-optic trap (MOT) has already been investigated [7]. This fermionic isotope is one of the highest-quality, neutral-atom-based optical frequency standards with accuracy below 10^{-18} s [8]. The distinctive property of this atomic clock is that the atoms are trapped at the magic wavelengths of an external laser field.

Determination of the magic wavelengths of alkali-metal atoms for linearly polarized [i.e., spin angular momentum (SAM) equal to zero] laser sources has been well explored in the literature [9,10]. Compared with linearly polarized light, circularly polarized light (i.e., SAM $= \pm 1$) has an extra part of the total polarizability called the "vector part" which arises due to the dipole moment perpendicular to the field. For circularly polarized light, this vector part has some advantages in the evaluation of the valence polarizability [11,12].

Most of the previous works in the area of trapping have assumed plane-wave or Gaussian modes of a laser. Kuga *et al.* [13] first realized Laguerre-Gaussian–based (LG-based) dipole traps and confined 10^8 rubidium atoms in the core of a blue-detuned vortex beam (see Fig. 1). Several recent experimental explorations of trapping atoms using LG light beams [14–16] suggest the importance of the process. The distinct spatial intensity profile of this LG beam carries a phase singularity on its axis [17,18]. This beam is associated with orbital angular momentum (OAM) due to the helical phase front [18,19]. As shown in Fig. 1, trapping of an atom is possible in the bright or dark region of an LG beam depending upon the sign of detuning. Apart from OAM, the LG beam also carries SAM associated with its polarization. During the interaction of a paraxial LG beam with atoms or ions, which is below its recoil limit, the lowest-order transition is possible at the quadrupole level [18,20] where the electronic motion is affected by the OAM of the LG beam. Therefore, the OAM of a paraxial LG beam does not influence dipole polarizability of an atomic state, but certainly has some effect on quadrupolar polarizability. Hence the dipole polarizability solely depends on the SAM of the paraxial LG beam. But the situation is different when the nonparaxial or focused circular LG beam is considered. Here, the SAM and OAM of the beam are coupled, and they are not conserved separately [19,21]. But the total angular momentum (=OAM + SAM) is conserved in interactions with atom [22,23]. In our recent work [19], we showed that, along with the SAM, the OAM of a focused LG beam can be transferred to the electronic motion of cold atoms in the dipole-approximation level. This leads to OAM- and

*analbhowmik@phy.iitkgp.ernet.in
†nnd0004@auburn.edu
‡sonjoym@phy.iitkgp.ernet.in

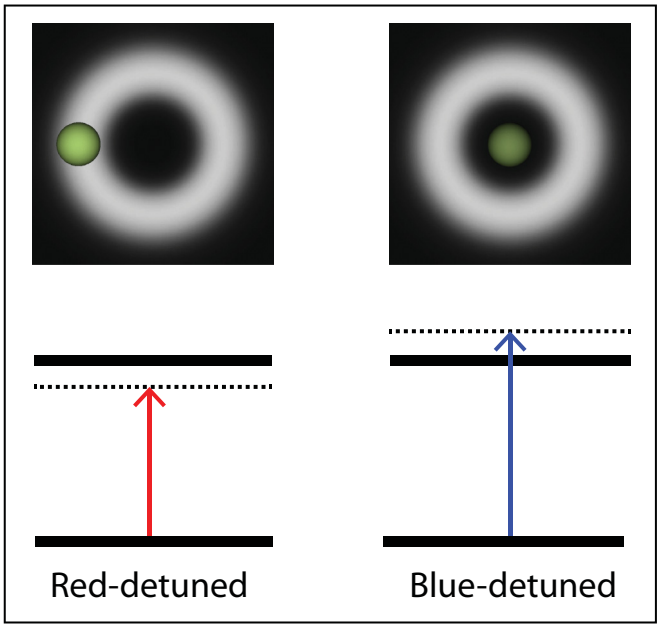

FIG. 1. The designs of trapping geometries to confine ions to regions of maximal or minimal light intensity for a red- or blue-detuned LG beam, respectively.

SAM-dependent dipole polarizability of an atomic state and magic wavelengths of a transition.

In this paper, we develop a theory to calculate the dynamic dipole polarizability of an atomic state with circularly polarized nonparaxial LG beam and apply this to determine magic wavelengths of the transitions $5s_{1/2} \rightarrow 4d_{3/2}, 4d_{5/2}$ of Sr^+ ions. We show how the OAM and SAM of a focused LG beam affect the dipole polarizability of an atomic state. The coupling of these two kinds of angular momentum increases with focusing angle. The impact of focusing angle on the dipole polarizability and magic wavelengths will be interesting to experimentalists, and we quantify this with our numerical calculations. We also found a number of magic wavelengths for which the ion can be confined to the nodes (blue-detuned) or antinodes (red-detuned) of the LG beam.

II. THEORETICAL FRAMEWORK

The second-order energy shift of an atom or ion placed in an external oscillating electric field $E(\omega)$ can be estimated from the time-independent perturbation theory as [24] $\Delta F(\omega) = -\frac{1}{2}\alpha(\omega)E^2$, where $\alpha(\omega)$ is the polarizability of the atomic or ionic energy state at frequency ω and E is the magnitude of the external electric field. For monovalent atomic systems with a valence electron in the vth orbital, the polarizability can be represented as

$$\alpha(\omega) = \alpha_c(\omega) + \alpha_{vc}(\omega) + \alpha_v(\omega). \tag{1}$$

Here, $\alpha_c(\omega)$ and $\alpha_v(\omega)$ are the frequency-dependent core polarizability of the ionic core (in the absence of the valence electron) and the valence polarizability of the single valence system, respectively. $\alpha_{vc}(\omega)$ represents the correction [25] to core polarizability due to presence of the valence electron and is considered ω independent due to tightly bound core electrons. The core polarizability of an atomic or ionic system can be estimated as [24,26,27]

$$\alpha_c(\omega) = \frac{2}{3}\sum_{ap} \times \frac{|\langle\Phi_a||D_{\rm DF}||\Phi_p\rangle\langle\Phi_a||D_{\rm RMBPT(2)}||\Phi_p\rangle|(\epsilon_p - \epsilon_a)}{(\epsilon_p - \epsilon_a)^2 - \omega^2}. \tag{2}$$

Here a and p represent all the core (occupied by electrons) and virtual orbitals (unoccupied by electrons), respectively. $\langle\Phi_a||D_{\rm DF}||\Phi_p\rangle$ and $\langle\Phi_a||D_{\rm RMBPT(2)}||\Phi_p\rangle$ are the reduced dipole matrix elements at the Dirac-Fock (DF) and the second-order relativistic many-body perturbation theory [RMBPT(2)] levels, respectively.

To calculate the valence polarizability $\alpha_v(\omega)$ of a monovalent system, we consider that a nonparaxial LG beam interacts with cold Sr^+ whose de Broglie wavelength is large enough to feel the intensity variation of the focused LG beam. Here, the nonparaxial beam is created from a circularly polarized LG beam by passing it through an objective (lens) with high numerical aperture [19]. The spot size of the paraxial LG beam is such that it overfills the entrance aperture radius of the objective to take full advantage of the high numerical aperture. Because of focusing and the diffraction from the edges of the objective, the SAM and OAM of the light get coupled and compose into a superposition of plane waves having an infinite number of spatial harmonics [28,29]. Here, we should mention that, whenever we refer SAM or OAM, it should be understood that we mean the corresponding angular momentum of the paraxial LG beam before passing through the objective lens. For a nonparaxial circularly polarized LG beam, the electric field in the laboratory coordinate system can be expressed as [19]

$$\begin{aligned}\mathbf{E} = E_0 e^{-i\omega t}\big[&I_0^{(l)}(r'_\perp,z')e^{il\Phi'}\{\hat{\mathbf{x}}(-i)^{l+1} + \hat{\mathbf{y}}\beta(-i)^l\} \\ &+ I_{2\beta}^{(l)}(r'_\perp,z')e^{i(l+2\beta)\Phi'}\{\hat{\mathbf{x}}(-i)^{l+1} - \hat{\mathbf{y}}\beta(-i)^l\} \\ &- (2\beta)(-i)^l I_\beta^{(l)}(r'_\perp,z')e^{i(l+\beta)\Phi'}\hat{\mathbf{z}}\big] + \text{c.c.},\end{aligned} \tag{3}$$

where β and ω are the polarization and frequency of light, respectively. The amplitude of the focused electric field is $E_0 = \frac{\pi f}{\lambda} T E_{\rm inc}$, where $E_{\rm inc}$ is the amplitude of the incident electric field, T is the transmission amplitude of the objective, and f is its focal length related to r' by $r' = f\sin\theta$ (Abbe sine condition). The coefficient $I_m^{(l)}$, where m takes the values 0, ±1, ±2 in the above expressions, depends on the focusing angle $\theta_{\rm max}$ by [19,23]

$$I_m^{(l)}(r'_\perp,z') = \int_0^{\theta_{\rm max}} d\theta \left(\frac{\sqrt{2}r'_\perp}{w_0\sin\theta}\right)^{|l|}(\sin\theta)^{|l|+1} \times \sqrt{\cos\theta}\, g_{|m|}(\theta) J_{l+m}(kr'_\perp\sin\theta)e^{ikz'\cos\theta}, \tag{4}$$

where $r'_\perp$ is the projection of $\boldsymbol{r}'$ on the xy plane, w_0 is the waist of the paraxial beam, and $J_{l+m}(kr'_\perp\sin\theta)$ is a cylindrical Bessel function. The angular functions are $g_0(\theta) = 1 + \cos\theta$, $g_1(\theta) = \sin\theta$, $g_2(\theta) = 1 - \cos\theta$. We consider that the incident beam has circular polarization with $\beta = \pm1$. Therefore, Eq. (3)

TABLE I. Calculated $E1$ transition amplitudes (in a.u.) and their comparison with other results (Others). The experimental ($\lambda_{\rm NIST}$) and RCC($\lambda_{\rm RCC}$) wavelengths are presented in Å. "Others" are calculated by using excitation energies from NIST [40] and the oscillator strengths presented in the references.

Transition	$\lambda_{\rm RCC}$	$\lambda_{\rm NIST}$	RCC	Others
$5s_{1/2} \rightarrow 5p_{1/2}$	4191.32	4216.88	3.1062	3.0903[a], 3.12[b]
$5s_{1/2} \rightarrow 5p_{3/2}$	4053.71	4079.05	4.38971	4.3704,[a] 4.40[b]
$4d_{3/2} \rightarrow 5p_{1/2}$	11439.88	10918.61	3.08262	3.1113,[a] 3.47(32)[c]
$4d_{3/2} \rightarrow 5p_{3/2}$	10469.81	10040.18	1.36854	1.3820,[a] 1.45(14)[c]
$4d_{3/2} \rightarrow 4f_{5/2}$	2172.71	2153.56	2.82947	2.9172[a]
$4d_{5/2} \rightarrow 5p_{3/2}$	10807.36	10329.25	4.1498	4.1833[a]
$4d_{5/2} \rightarrow 4f_{5/2}$	2186.88	2166.57	0.76694	0.7887[a]
$4d_{5/2} \rightarrow 4f_{7/2}$	2186.95	2166.59	3.43082	3.5214[a]

[a]Theoretical [37].
[b]Experimental [38].
[c]Experimental [39].

becomes

$$\begin{aligned}\mathbf{E} = E_0 e^{-i\omega t}\big[&\sqrt{2}(-i)^{l+1} I_0^{(l)} e^{il\Phi'}\hat{\boldsymbol{\epsilon}}_{\boldsymbol{\beta}} \\ &+ \sqrt{2}(-i)^{l+1} I_{+2}^{(l)} e^{i(l+2)\Phi'}\hat{\boldsymbol{\epsilon}}_{-\boldsymbol{\beta}} \\ &\mp 2(-i)^{l} I_{\pm 1}^{(l)} e^{i(l\pm 1)\Phi'}\hat{\mathbf{z}}\big] + \text{c.c.},\end{aligned} \tag{5}$$

where the polarization vector $\hat{\boldsymbol{\epsilon}}_{\boldsymbol{\beta}} = \frac{\hat{\mathbf{x}}+i\beta\hat{\mathbf{y}}}{\sqrt{2}}$. To make the equation simpler, we have written $I_m^{(l)}(r'_\perp, z')$ as $I_m^{(l)}$. Since focusing of the LG beam has created three types of local polariztion (right circular, left circular, and linear) [19], therefore, to conserve the total angular momentum in each of the parts of Eq. (5), OAM should be modified accordingly. Hence, $\alpha_v(\omega)$ should have the cumulative effect of all three polarized parts of the electric field. Now, using Eq. (5), $\alpha_v(\omega)$ will take the form of

$$\begin{aligned}\alpha_v(\omega) = &\, 2A_0\alpha_v^0(\omega) + 2\left(\frac{m_J}{2J_v}\right)A_1\alpha_v^1(\omega) \\ &+ 2\left(\frac{3m_J^2 - J_v(J_v+1)}{2J_v(2J_v-1)}\right)A_2\alpha_v^2(\omega),\end{aligned} \tag{6}$$

where J_v is the total angular momentum of state ψ_v and m_j is the magnetic component. The parameters A_i are defined as $A_0 = [\{I_0^{(l)}\}^2 + \{I_{+2}^{(l)}\}^2 + 2\{I_{\pm 1}^{(l)}\}^2]$, $A_1 = [\pm\{I_0^{(l)}\}^2 \mp \{I_{+2}^{(l)}\}^2]$, and $A_2 = [\{I_0^{(l)}\}^2 + \{I_{+2}^{(l)}\}^2 - 2\{I_{\pm 1}^{(l)}\}^2]$. $\alpha_v^0(\omega)$, $\alpha_v^1(\omega)$, and $\alpha_v^2(\omega)$ are the scalar, vector, and tensor parts, respectively, of the valence polarization and can be written as [24,27]

$$\alpha_v^0(\omega) = \frac{2}{3(2J_v+1)}\sum_n \frac{|\langle\psi_v||d||\psi_n\rangle|^2(\epsilon_n - \epsilon_v)}{(\epsilon_n-\epsilon_v)^2 - \omega^2}, \tag{7}$$

$$\begin{aligned}\alpha_v^1(\omega) = -\sqrt{\frac{6J_v}{(J_v+1)(2J_v+1)}}\sum_n (-1)^{J_n+J_v}\begin{Bmatrix} J_v & 1 & J_v \\ 1 & J_n & 1\end{Bmatrix} \\ \times \frac{|\langle\psi_v||d||\psi_n\rangle|^2(2\omega)}{(\epsilon_n-\epsilon_v)^2-\omega^2},\end{aligned} \tag{8}$$

and

$$\begin{aligned}\alpha_v^2(\omega) = 4\sqrt{\frac{5J_v(2J_v-1)}{6(J_v+1)(2J_v+1)(2J_v+3)}} \\ \times \sum_n (-1)^{J_n+J_v}\begin{Bmatrix} J_v & 1 & J_n \\ 1 & J_v & 2\end{Bmatrix} \\ \times \frac{|\langle\psi_v||d||\psi_n\rangle|^2(\epsilon_n-\epsilon_v)}{(\epsilon_n-\epsilon_v)^2-\omega^2}.\end{aligned} \tag{9}$$

Therefore, $\alpha_v(\omega)$ directly depends on different combinations of integrals $I_m^{(l)}$. In addition, these integrals can be modified by changing the combination of SAM and OAM of the incident LG beam and the numerical aperture of the objective. There-

TABLE II. Static valence scalar (α_v^0) and static tensor (α_v^2) polarizabilities (in a.u.) for the states $5s_{1/2}$, $4d_{3/2}$, and $4d_{5/2}$ and their comparisons with the other results (Others).

	α_v^0		α_v^2	
State	Present	Others	Present	Others
$5s_{1/2}$	87.68	86.374,[a] 85.75[b] 85.75,[c] 87.5[d]		
$4d_{3/2}$	55.92	57.87,[a] 58.78[b] 51.20[d]	−34.67	−35.50(6),[a] −35.26[b]
$4d_{5/2}$	56.21	56.618,[a] 57.11[b] 56.59,[c] 51.20[d]	−47.12	−47.70(8),[a] −47.35[b] −47.70(3)[c]

[a]Safronova [37].
[b]Jiang *et al.* [43].
[c]Experimental [39].
[d]Barklem and O'Mara [44].

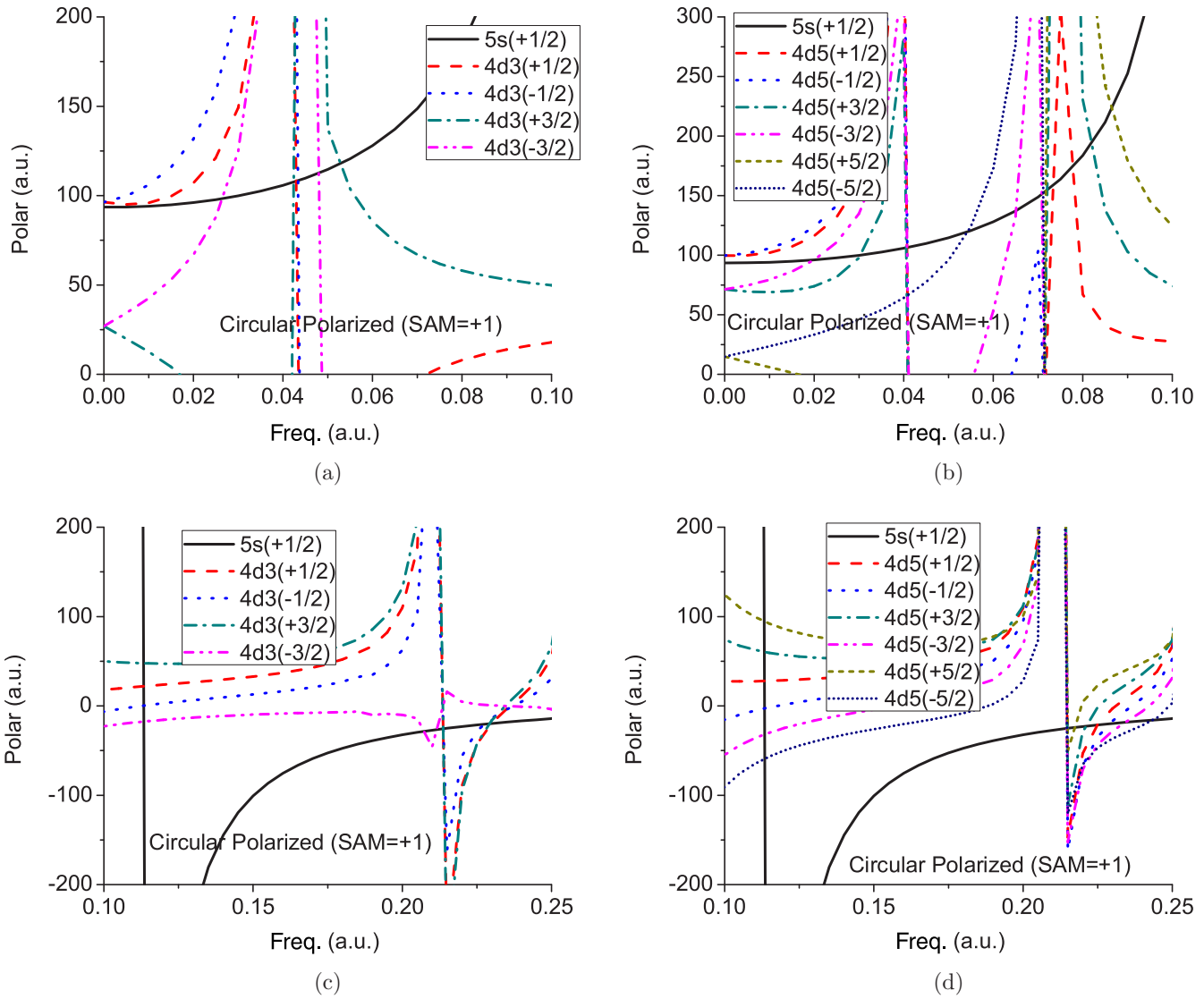

FIG. 2. Frequency (Freq.) dependence of polarizabilities (Polar) for the $5s_{\frac{1}{2}}$ and $4d_{\frac{3}{2},\frac{5}{2}}$ states for circular polarized Gaussian light with SAM $= +1$. The brackets indicate the magnitudes of the magnetic components. Panels (a) and (c) are for the $5s_{\frac{1}{2}}$ and $4d_{\frac{3}{2}}$ states and panels (b) and (d) are for the $5s_{\frac{1}{2}}$ and $4d_{\frac{5}{2}}$.

fore, the polarizability can also be tuned with the focusing angle of the nonparaxial LG beam.

III. NUMERICAL RESULTS AND INTERPRETATIONS

The major aim of this work is to calculate precise values of magic wavelengths associated with the $5s_{1/2} \rightarrow 4d_{3/2}, 4d_{5/2}$ transitions of Sr^+ ion. Therefore, as stated earlier, we need to estimate dynamic polarizabilities of the $5s_{1/2}$, $4d_{3/2}$, and $4d_{5/2}$ states of this ion for different magnetic sublevels. Using Eqs. (7)–(9), one can calculate the scalar, vector, and tensor parts of the valence polarizabilities, respectively, for the associated valence configurations of these states. The precise estimations of $E1$ transition amplitudes and corresponding transition energies highlight the accuracy of our calculations. To evaluate these quantities, we use a relativistic coupled cluster (RCC) theory having wave operators associated with single and double and valence triple excitations in linear and nonlinear forms. This is similar to the spirit of CCSD(T) [30], which is used by many quantum chemists. Our RCC wave functions, based on the corresponding DF wave functions, produce highly precise $E1$ transition amplitudes as discussed in our earlier work [31–36].

Table I presents a comparison of the most important reduced dipole matrix elements as calculated by us with the corresponding theoretical results of Safronova [37] and some experimental measurements [38,39]. Safronova estimated the results by using an all-order single-double with partial triple (SDpT) excitations method in a linearized approximation. The small difference between the results come from the addition of some nonlinear terms in our present theory. Also, Safronova used B-spline bases to construct the Dirac-Fock orbitals, whereas we consider Gaussian-type orbital (GTO) bases to generate these orbitals. The table also includes a comparison of the wavelengths of the transitions calculated by our RCC method with the corresponding wavelengths as obtained from

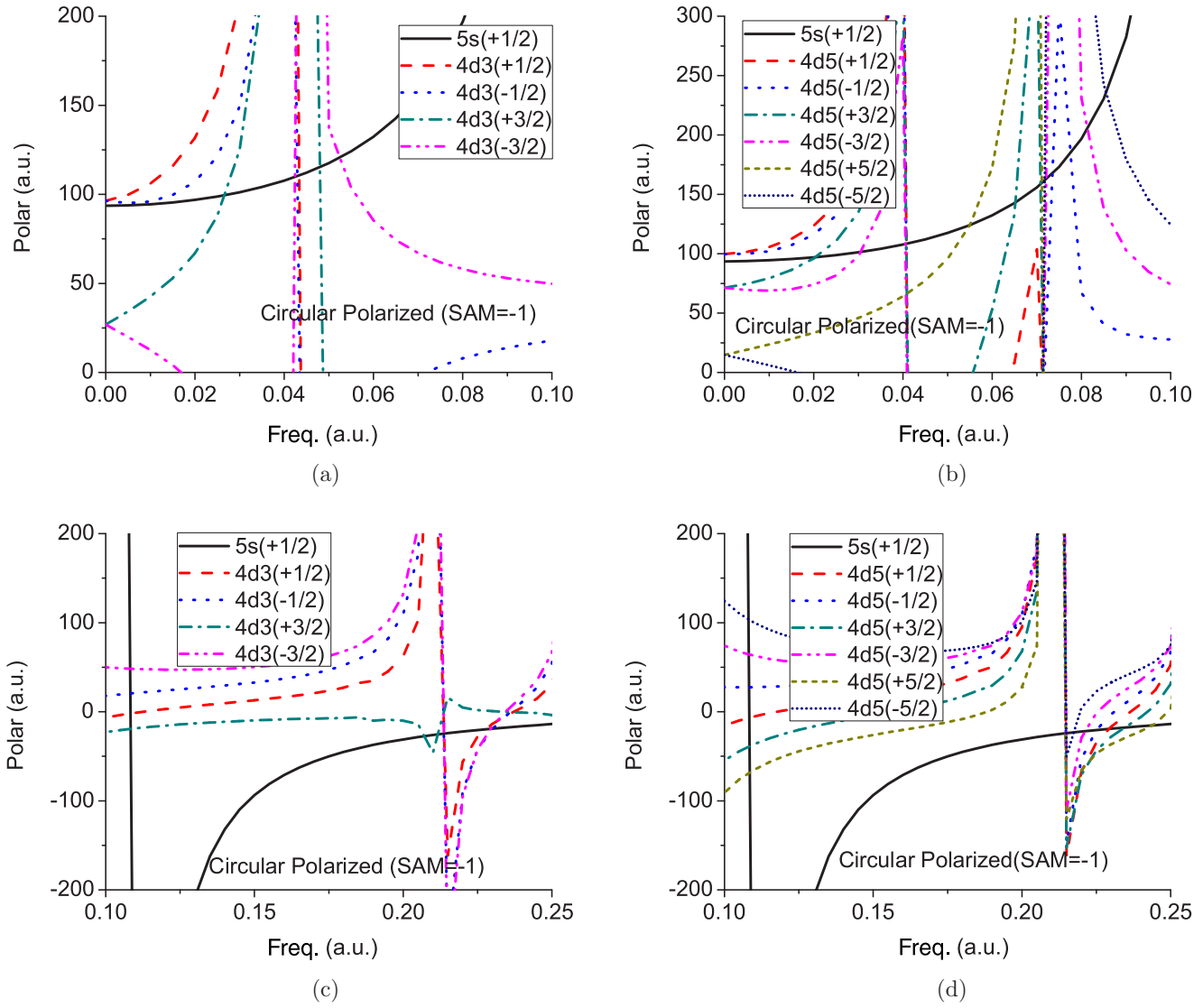

FIG. 3. Frequency (Freq.) dependence of polarizabilities (Polar) for the $5s_{\frac{1}{2}}$ and $4d_{\frac{3}{2},\frac{5}{2}}$ states for circular polarized Gaussian light with SAM $= -1$. The brackets indicate the magnitudes of the magnetic components. Panels (a) and (c) are for the $5s_{\frac{1}{2}}$ and $4d_{\frac{3}{2}}$ states and panels (b) and (d) are for the $5s_{\frac{1}{2}}$ and $4d_{\frac{5}{2}}$.

the National Institute of Standards and Technology (NIST) [40].

To calculate the required polarizabilities for $5s_{\frac{1}{2}}$, $4d_{\frac{3}{2}}$, and $4d_{\frac{5}{2}}$ states, we use Eqs. (1), (2), (6)–(9). The ionic core polarizability $\alpha_c(\omega)$ is irrespective of the position of valence electrons and can be calculated quite accurately by using Eq. (2). The valence polarizability needs the most attention because it can be affected significantly by the electron-correlation due to loser binding of a valence electron to the nucleus. The $E1$ matrix elements present in the valence polarizability expressions [Eqs. (7)–(9)] are considered at different levels of theoretical considerations depending on their significance to the sum. The most dominant and therefore important contributions to the valence polarizabilities come from the parts of the sums in Eqs. (7)–(9) which are involved with the intermediate states in the ranges of $5\,^2P$–$8\,^2P$ and $4\,^2F$–$6\,^2F$. Therefore, the $E1$ matrix elements associated with these intermediate states are calculated by using the correlation exhaustive RCC method. RMBPT(2) [41], which includes core-polarization correction on top of the DF approximation, is used to calculate the comparatively less significant $E1$ matrix elements in the polarizability expressions with intermediate states from $9\,^2P$–$12\,^2P$ and $7\,^2F$–$12\,^2F$. The intermediate states with $n = 13$ to 25 in Eqs. (7)–(9) contribute by a small value, and therefore, without loss of significant accuracy to the polarizability value, they are computed by using the DF wave functions. For n greater than 25, the sums are expected to contribute by a very little amount and thus are neglected. To obtain better accuracy in calculating a total polarizability value, we have used the experimental transition energies [40] to calculate the most dominant part of corresponding valence polarizability.

In Table II, we compare static values of valence scalar and tensor polarizabilities for the $5s_{\frac{1}{2}}$ and $4d_{\frac{3}{2},\frac{5}{2}}$ states with the theoretical [37,42,43] and experimental [44] values as available in the literature. Both Jiang *et al.* [43] and Safronova [37] adopted almost a similar strategy in calculations of the

TABLE III. Magic wavelengths (in nm) of Sr^+ for linearly and circularly polarized Gaussian light for the transitions $5s_{1/2}(+1/2) \rightarrow 4d_{3/2}(m_J)$ and $5s_{1/2}(+1/2) \rightarrow 4d_{5/2}(m_J)$.

Circularly polarized (SAM = +1)						Circularly polarized (SAM = −1)						Linearly polarized		
State (J,m_J)	λ_{magic}	α	State (J,m_J)	λ_{magic}	α	State (J,m_J)	λ_{magic}	α	State (J,m_J)	λ_{magic}	α	State (J,m_J)	λ_{magic}	α
$(\frac{3}{2},+\frac{1}{2})$	1062.08	107.96	$(\frac{3}{2},-\frac{1}{2})$	1054.71	108.71	$(\frac{3}{2},+\frac{1}{2})$	1052.27	110.54	$(\frac{3}{2},-\frac{1}{2})$	1059.61	110.52	$(\frac{3}{2},\|\frac{1}{2}\|)$	1052.27	109.51
	402.15	22.06		402.15	0.51		420.33	−2.29		421.10	20.05		406.82	10.96
	212.81	−24.13		212.81	−24.13		420.33	−2.29		212.91	−24.63		212.91	−24.63
	198.19	−19.72		200.28	−20.45		200.10	−19.59		197.76	−18.56		198.53	−19.65
$(\frac{3}{2},+\frac{3}{2})$	1072.08	107.96	$(\frac{3}{2},-\frac{3}{2})$	1732.45	98.34	$(\frac{3}{2},+\frac{3}{2})$	1739.06	99.37	$(\frac{3}{2},-\frac{3}{2})$	1072.08	109.28	$(\frac{3}{2},\|\frac{3}{2}\|)$	1130.60	106.99
	861.31	118.16		953.21	112.54		949.24	115.06		869.53	120.9		929.86	115.06
	402.15	46.64		402.15	−18.04		420.33	−19.59		421.49	48.45		406.82	15.22
	212.81	−24.13		220.43	−27.37		220.01	−27.72		212.91	−24.63		213.31	−25.54
	198.79	−19.98		215.33	−25.75		215.43	−25.66		198.19	−18.56		202.86	−20.40
$(\frac{5}{2},+\frac{1}{2})$	1119.49	106.44	$(\frac{5}{2},-\frac{1}{2})$	1119.49	106.44	$(\frac{5}{2},+\frac{1}{2})$	1125.02	107.90	$(\frac{5}{2},-\frac{1}{2})$	1125.02	107.90	$(\frac{5}{2},\|\frac{1}{2}\|)$	1119.49	107.13
	621.60	158.93								619.91	167.27			
	585.65	174.91								588.67	184.45			
	402.15	27.79		402.15	−2.56		420.33	−6.41		421.49	28.18		407.18	12.15
	212.12	−25.27		212.12	−25.27		212.02	−24.63		212.02	−24.63		212.02	−24.82
	202.68	−21.38		198.79	−20.10		198.53	−18.56		202.32	−20.62		200.72	−20.31
$(\frac{5}{2},+\frac{3}{2})$	1513.73	99.57	$(\frac{5}{2},-\frac{3}{2})$	2301.18	95.79	$(\frac{5}{2},+\frac{3}{2})$	2278.17	96.48	$(\frac{5}{2},-\frac{3}{2})$	1503.74	101.12	$(\frac{5}{2},\|\frac{3}{2}\|)$	1793.83	99.14
	1119.49	105.67		1119.49	106.44		1125.02	107.9		1125.02	107.9		1119.49	107.13
	631.95	155.15		700.97	137.63		698.82	143.73		631.07	163.83			
	556.33	194.67		642.64	151.29		644.46	159.28		561.13	205.76			
	402.15	60.94		402.15	−32.60		420.33	−39.86		422.27	64.72		407.18	14.02
	212.12	−25.27		212.12	−25.27		212.02	−24.63		212.02	−24.63		212.02	−24.82
	205.98	−22.69		194.38	−18.37		194.13	−17.53		205.89	−21.08		202.05	−20.73
$(\frac{5}{2},+\frac{5}{2})$	637.25	152.84	$(\frac{5}{2},-\frac{5}{2})$	839.10	120.10	$(\frac{5}{2},+\frac{5}{2})$	831.45	123.88	$(\frac{5}{2},-\frac{5}{2})$	635.47	161.94	$(\frac{5}{2},\|\frac{5}{2}\|)$		
	526.74	222.85		642.64	152.06		640.83	159.71		532.90	235.05			
	402.15	94.25		402.15	−59.68		420.33	−68.27		421.49	104.23		407.18	17.66
	212.12	−25.27		212.12	−25.27		212.02	−24.63		212.02	−24.63		212.02	−24.82
	209.58	−24.00		187.12	−15.79		186.66	−15.46		209.68	−22.57		204.96	−21.85

most dominant contributor to their total polarizability values, i.e., the valence polarizabilities. They used an approximately similar kind of all-order relativistic many-body perturbation method where single, double, and partial triple excitations in this method are considered in linear form. As mentioned earlier, the present approach accounts for these excitations in both linear and nonlinear forms. Also, both of them applied the random-phase approximation (RPA) to calculate the core polarizability, whereas we use RMBPT(2) to estimate the core polarizability. Kaur *et al.* applied a relativistic coupled-cluster method with single and double excitations to compute dominant portions of the valence polarizabilities of the ground and excited states [42]. However, they used the same RPA approximation as used by Jiang *et al.* and Safronova to calculate the core polarizability. All the theoretical calculations are in very close agreement for core and core-valence parts of the corresponding total polarizabilities. The computed static core polarizability $\alpha_c(0)$ of the ion is 6.103 a.u., and the static core-valence parts $\alpha_{vc}(0)$ of the polarizabilities for the states $5s_{\frac{1}{2}}$, $4d_{\frac{3}{2}}$, and $4d_{\frac{5}{2}}$ are −0.25, −0.38, and −0.42 a.u., respectively. In Table II, we compare only valence parts of the corresponding static polarizabilities among the estimates from different calculations. The experimental measurement of Barklem and O'Mara [44] shows a difference in the valence polarizability of the $5s_{\frac{1}{2}}$ state by around 0.2%. Nevertheless, the agreements of our calculated energies, amplitudes of $E1$ transitions, static values of scalar and tensor polarizabilities with the estimates by other theoretical and experimental groups can indicate a good calibration of our present calculations. We can claim now that our present approach of calculating dynamic polarizability is accurate enough to study the effect of focused LG beams on Sr^+ in terms of magic wavelengths.

For the sake of comparison with the LG beam, we have first plotted the dynamical polarizability of the $5s_{\frac{1}{2}}$ and $4d_{\frac{3}{2},\frac{5}{2}}$ states of Sr^+ with the frequency of circularly polarized Gaussian light in Figs. 2 and 3. This is extremely important for many high-precision experiments in quantum optics, especially, identifications of magic wavelengths correspond to high polarization. A point to be noted from the two figures is that variation path of polarizabilities exchanged between states with (J,m_J) and $(J,-m_J)$ by changing the direction of polarization of light, as expected. However, only one estimate is found in the literature [42] with one of the possible magic wave numbers which is not even for a high polarizability. The analysis in the broad range of magic frequencies including the one corresponding to the highest polarizability presented in Figs. 2 and 3. The actual values of the magic wavelengths and corresponding polarizabilities due to circular and linearly polarized light are tabulated in Table III. One can see that there are multiple magic wavelengths found in the presented frequency range for

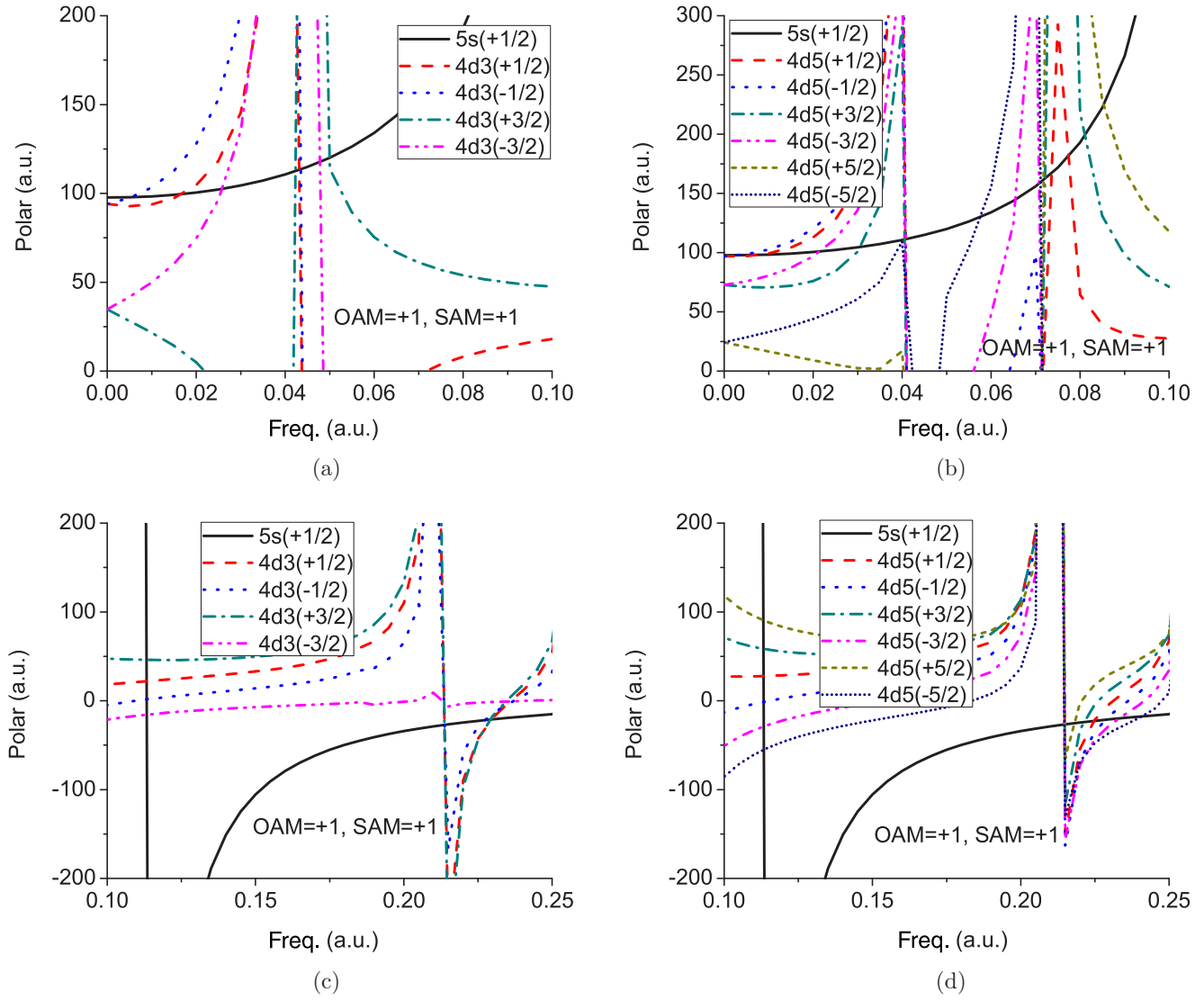

FIG. 4. Frequency (Freq.) dependence of polarizabilities (Polar) for the $5s_{\frac{1}{2}}$ and $4d_{\frac{3}{2}}$,$4d_{\frac{5}{2}}$ states for the focused (50°) LG beam with OAM = +1 and SAM = +1. The brackets indicate the magnitudes of the magnetic components. Panels (a) and (c) are for the $5s_{\frac{1}{2}}$ and $4d_{\frac{3}{2}}$ states, and panels (b) and (d) are for the $5s_{\frac{1}{2}}$ and $4d_{\frac{5}{2}}$ states.

the transitions between the magnetic sublevels of $5s_{\frac{1}{2}}$ and the magnetic sublevels of $4d_{\frac{3}{2},\frac{5}{2}}$ states. The tabulated magic wavelengths fall in the near-infrared, visible, and UV regions of the frequency spectrum. All the magic wavelengths which belong to the visible and UV regions favor blue-detuned trapping, and those which belong to the near-infrared region support red-detuned trapping. In some cases, no magic wavelength is found for a particular range of the spectrum, and we keep the slot as blank in the Table II and tables henceforth.

In Figs. 4 and 5, we present the plots of the dynamic polarizabilities of $5s_{\frac{1}{2}}$, $4d_{\frac{3}{2}}$, and $4d_{\frac{5}{2}}$ states considering the external field of nonparaxial LG beam which is focused at angle of 50°. Here, we have chosen angular momenta of the incident beam as (OAM,SAM) = (+1,+1) and (+1,−1) to demonstrate their dependencies on the polarizabilities. The maximum polarizabilities observed in these plots correspond to the polarizabilities at the resonance transitions. For the $5s_{1/2}$, $4d_{3/2}$, and $4d_{5/2}$ states, the resonances occur due to the $5s_{1/2} \rightarrow 5p_{1/2},5p_{3/2}$, $4d_{3/2} \rightarrow 5p_{1/2},5p_{3/2}$, and $4d_{5/2} \rightarrow 5p_{3/2}$ transitions, respectively, in the chosen spectral range. These figures show a number of crossings of the polarizabilities of $5s_{\frac{1}{2}}$ and multiplets of $4d_{\frac{3}{2}}$ and $4d_{\frac{5}{2}}$ states. These crossings indicate magic wavelengths of the externally focused LG field for which the transition wavelengths between $5s_{\frac{1}{2}}$, $4d_{\frac{3}{2}}$, and $4d_{\frac{5}{2}}$ states remain unaffected. There have been remarkable differences of polarizability observed compared with Gaussian beams in the low-frequency region. Significant changes observed for interaction with a right circularly polarized LG beam and found extra magic wavelength for $(J,m_J) = (3/2, \pm 1/2)$ in the near-infrared region. Other changes are clear from the comparisons of the polarization plots presented in Figs. 4 and 5 with Figs. 2 and 3 and obvious from magic wavelengths tabulated in Tables IV–VI for different focusing angles (50°, 60°, and 70°) and the combination of OAM and SAM [(+1,+1), (+1,−1), (+2,+1), and (+2,−1)] with Table III. Since the OAM and SAM are coupled in case of nonparaxial LG beam

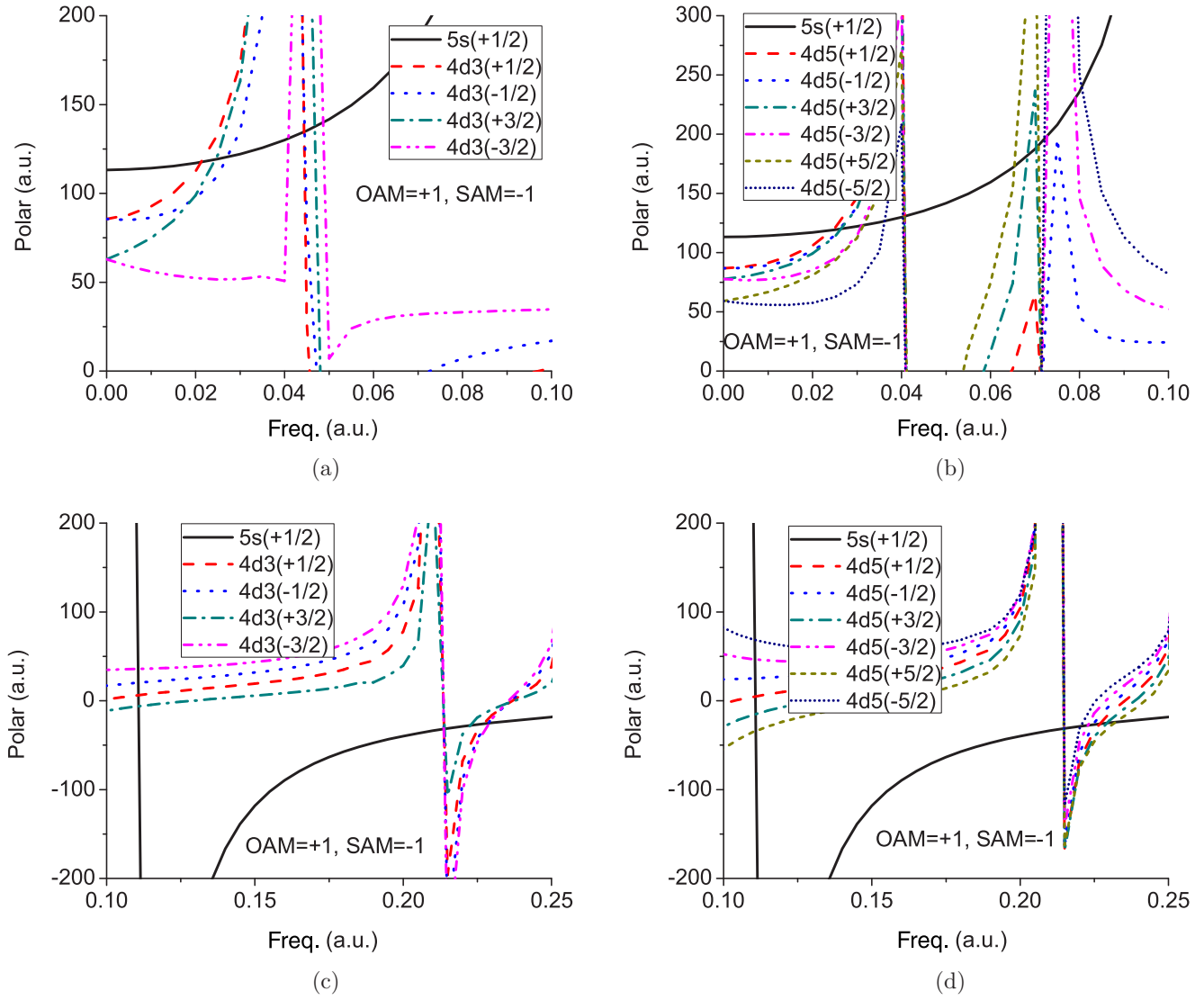

FIG. 5. Frequency (Freq.) dependence of polarizabilities (Polar) for the $5s_{\frac{1}{2}}$ and $4d_{\frac{3}{2}}$,$4d_{\frac{5}{2}}$ states for the focused (50°) LG beam with OAM $= +1$ and SAM $= -1$. The brackets indicate the magnitudes of the magnetic components. Panels (a) and (c) are for the $5s_{\frac{1}{2}}$ and $4d_{\frac{3}{2}}$ states, and panels (b) and (d) are for the $5s_{\frac{1}{2}}$ and $4d_{\frac{5}{2}}$ states.

and more focusing yields stronger coupling, from our previous experience with focused LG beams [19], we expect the changes of values of magic wavelengths should be appreciable for the chosen large focusing angles of the beam. The presented magic wavelengths in the tables span from the infrared to ultraviolet (UV) region in the energy spectrum. It is interesting to note that the effects of focusing angles are appreciable for larger magic wavelengths. Also, for those wavelengths, the values of magic wavelengths reduce significantly with the increase of focusing angles, but the polarizabilities increase. Our study shows that the change of polarization with focusing angle is very small for the $5s_{\frac{1}{2}}$ state. Therefore, the changes of magic wavelengths seen in the tables are mostly due to the variation of polarizabilities of the $4d_{\frac{3}{2}}$ and $4d_{\frac{5}{2}}$ states. This phenomenon is significant for trapping of atoms or ions, because magic wavelengths with large polarizabilities will be more helpful to experimentalists for trapping. In the range of our chosen spectrum, we find a set of five magic wavelengths for $5s_{\frac{1}{2}}$ to $4d_{\frac{3}{2}}$ and $4d_{\frac{5}{2}}$ transitions for all the considered combinations of OAM, SAM, and focusing angles apart from a few cases.

Tables IV–VI show that the infrared or near-infrared magic wavelength regions of the energy spectrum have larger values of polarizabilities compared with the visible and UV regions. Therefore, the magic wavelengths in the infrared or near-infrared region are highly recommended for trapping by using a red-detuned trap (see Fig. 1), where the ions can be trapped in the region of high intensity of the LG beam [16,45]. Also, the magic wavelengths and the corresponding polarizabilities at these regions show significant variation with focusing angle and choice of initial OAM and SAM compared with the same in the visible and UV region. In other words, we can tune the magic wavelengths here by the external parameters of light. Since the wavelength of the resonance transitions $5s_{\frac{1}{2}} \rightarrow 4d_{\frac{3}{2}}$,$4d_{\frac{5}{2}}$ are 687 nm and 674 nm, all the magic wavelengths in the visible and UV regions as shown in the tables support the blue-detuned trapping scheme. Therefore,

TABLE IV. Magic wavelengths (in nm) of Sr^+ for different focusing angles of the LG beam for the transitions $5s_{1/2}(+1/2) \rightarrow 4d_{3/2}(m_J)$.

Nonparaxial LG beam													
State $[4d_{3/2}(m_J)]$	$\lambda^{50^\circ}_{\rm magic}$	α	$\lambda^{60^\circ}_{\rm magic}$	α	$\lambda^{70^\circ}_{\rm magic}$	α	State $[4d_{3/2}(m_J)]$	$\lambda^{50^\circ}_{\rm magic}$	α	$\lambda^{60^\circ}_{\rm magic}$	α	$\lambda^{70^\circ}_{\rm magic}$	α
	OAM $= +1$, SAM $= +1$							OAM $= +1$, SAM $= -1$					
$(+1/2)$	2744.78	99.89	2255.61	104.12	2016.08	109.02	$(+1/2)$	2149.21	117.64	2090.06	118.56	1998.39	120.88
	1057.15	113.06	1045.03	118.00	1040.26	121.99		1028.52	134.88	1019.31	136.08	1023.90	137.63
	403.57	21.93	404.65	21.49	405.01	21.58		409.74	6.54	408.27	7.18	406.09	8.17
	213.11	−26.69	213.01	33.33	213.21	−29.70		213.11	−31.77	212.91	−32.02	213.21	−32.84
	198.45	−21.03	198.62	−21.99	198.88	−23.18		200.63	−25.95	200.63	−26.39	200.63	−26.70
$(-1/2)$	8933.99	97.82	4952.54	101.80	3301.69	109.02	$(-1/2)$	1693.80	120.16	1656.85	122.42	1644.89	123.88
	1047.43	113.58	1042.64	117.78	1042.64	122.42		1023.90	134.88	1019.31	136.08	1014.77	137.63
	403.57	1.24	404.65	1.94	404.65	3.47		410.11	20.48	408.27	20.30	406.45	20.19
	213.11	−26.69	213.01	33.33	213.21	−29.70		213.11	−31.77	212.91	−32.02	213.21	−32.84
	200.37	−21.80	200.54	−22.65	200.63	−23.91		199.23	−25.35	199.31	−25.66	199.40	−26.23
$(+3/2)$	1084.84	112.54	1077.15	116.32	1087.43	120.10	$(+3/2)$	1859.73	119.13	1859.73	120.88	1844.67	122.42
	911.27	120.16	914.93	123.88	920.47	128.09		973.58	137.92	977.75	139.52	977.75	140.64
	403.93	45.95	405.01	44.78	405.01	41.99		409.37	−6.02	407.91	−4.47	406.09	−2.76
	213.11	−26.69	213.01	33.33	213.21	−29.70		213.11	−31.77	212.91	−32.02	213.21	−32.84
	198.79	−21.15	198.79	−22.12	198.79	−22.92		204.60	−27.80	204.14	−27.88	203.68	−28.24
$(-3/2)$	1772.89	102.40	1786.80	105.67	1815.27	109.45	$(-3/2)$	1111.30	130.81	1133.42	131.53	1195.89	131.53
	953.21	117.64	957.21	120.88	961.25	125.43		937.52	139.46	937.52	141.41	941.39	142.96
	403.57	−16.16	404.29	−14.23	404.65	−11.65		410.48	35.78	408.64	34.49	406.82	33.09
					212.61	−28.10		213.11	−31.77	212.91	−32.02	213.21	−32.84
					208.62	−26.51		198.97	−25.21	198.97	−25.39	199.05	−26.07
	OAM $= +2$, SAM $= +1$							OAM $= +2$, SAM $= -1$					
$(+1/2)$	2531.30	100.86	2129.13	106.79	1815.27	113.57	$(+1/2)$	2129.13	118.61	2061.69	120.10	1963.94	121.31
	1057.15	115.06	1052.27	120.10	1042.64	126.20		1023.90	135.91	1023.90	136.86	1014.77	139.18
	405.01	21.92	404.65	21.68	405.01	21.35		409.37	6.63	407.18	7.66	406.45	8.58
	213.31	−27.49	213.11	−28.01	213.21	−30.27		213.21	−31.35	213.01	−32.78	213.21	−33.25
	198.45	−21.44	198.71	−22.62	198.97	−24.35		200.63	−26.10	200.72	−26.58	200.72	−26.94
$(-1/2)$	6603.38	99.37	3828.85	103.35	2761.42	109.45	$(-1/2)$	1662.90	121.19	1656.85	122.42	1633.10	125.00
	1047.43	115.58	1045.03	120.10	1042.64	126.20		1023.90	135.62	1023.90	136.86	1010.27	139.52
	404.65	1.40	404.65	3.07	404.65	4.77		409.74	20.45	407.54	20.34	406.45	19.94
	213.31	−27.49	213.11	−28.01	213.21	−30.27		213.21	−31.35	213.01	−32.78	213.21	−33.25
	200.45	−22.04	200.54	−23.37	200.72	−24.64		199.31	−25.54	199.40	−25.90	199.58	−26.50
$(+3/2)$	1082.26	113.57	1082.26	117.78	1092.65	124.31	$(+3/2)$	1859.73	119.87	1867.35	121.65	1844.67	122.42
	914.93	121.19	918.62	126.20	926.08	131.53		973.58	137.92	979.86	139.52	977.75	141.41
	405.01	45.54	405.01	43.71	405.01	40.32		409.37	−5.20	407.18	−3.70	406.09	−1.75
	213.31	−27.49	213.11	−28.01	213.21	−30.27		213.21	−31.35	213.01	−32.78	213.21	−33.25
	198.79	−21.44	198.79	−22.62	198.97	−24.35		204.50	−27.86	203.95	−28.01	203.41	−28.29
$(-3/2)$	1766.02	103.89	1808.07	107.13	1837.23	112.46	$(-3/2)$	1119.49	131.56	1141.94	132.65	1238.13	130.76
	953.21	119.13	957.21	123.88	965.33	129.64		935.59	139.98	945.30	141.41	947.26	142.96
	404.65	−15.26	404.65	−13.11	404.65	−9.99		410.11	35.50	407.91	33.94	406.82	32.17
			212.22	−28.01	212.71	−29.97		213.21	−31.35	213.01	−32.78	213.21	−33.25
			209.97	−28.01	207.58	−27.62		198.97	−25.36	199.05	−25.89	199.14	−26.31

these wavelengths seek the ion to confine in the low-intensity region of the LG beam [13,16,45,46] (see Fig. 1). However, there are few cases where optical magic wavelengths are larger than these resonance-transition wavelengths and support red-detuned trapping. They are 696.69, 694.56, and 688.27 nm (for OAM $= +1$) as shown in Table V, and 696.69, 692.45, and 682.09 nm (for OAM $= +2$) as shown in Table VI. The same situation appears in case of SAM $= -1$ but when the magnetic component of the final state is $m_J = +5/2$.

Because our main focus in this present work is on the magic wavelengths, we give a rough estimate of the theoretical uncertainty in the calculated magic wavelength values only. Here we recalculate the magic wavelengths (of all in Tables III–VI) by replacing our present RCC values of the most important $E1$ matrix elements by the corresponding SDpT values as calculated by Safronova [37]. These most important $E1$ matrix elements include $5s_{\frac{1}{2}} \rightarrow 5p_{\frac{1}{2}}, 5p_{\frac{3}{2}}$ transitions for the $5s_{\frac{1}{2}}$ state; $4d_{\frac{3}{2}} \rightarrow 5p_{\frac{1}{2}}, 5p_{\frac{3}{2}}$, and $4d_{\frac{3}{2}} \rightarrow 4f_{\frac{5}{2}}$ transitions for the $4d_{\frac{3}{2}}$ state; $4d_{\frac{5}{2}} \rightarrow 5p_{\frac{3}{2}}$ and $4d_{\frac{5}{2}} \rightarrow 4f_{\frac{5}{2}}, 4f_{\frac{7}{2}}$ transitions for the $4d_{\frac{5}{2}}$ state. The maximum of the relative differences between these recalculated wavelengths and the corresponding actual wavelengths (as presented in Tables III–VI) is $\pm 1\%$ and is considered as the theoretical uncertainty in our calculated magic wavelength values.

TABLE V. Magic wavelengths (in nm) of Sr^+ for different focusing angles of the LG beam for the transitions $5s_{1/2}(+1/2) \rightarrow 4d_{5/2}(m_J)$.

	Nonparaxial LG beam											
State $[4d_{5/2}(m_J)]$	$\lambda^{50^\circ}_{\rm magic}$	α	$\lambda^{60^\circ}_{\rm magic}$	α	$\lambda^{70^\circ}_{\rm magic}$	α	State $[4d_{5/2}(m_J)]$	$\lambda^{50^\circ}_{\rm magic}$	α	$\lambda^{60^\circ}_{\rm magic}$	α	$\lambda^{70^\circ}_{\rm magic}$	α
	OAM $= +1$, SAM $= +1$							OAM $= +1$, SAM $= -1$					
$(+1/2)$	7855.75	98.02	3057.94	101.80	2348.63	107.13	$(+1/2)$	1844.67	118.56	1815.27	120.10	1766.02	122.42
	1119.49	111.77	1119.49	114.78	1119.80	119.33		1116.75	130.76	1111.30	133.08	1119.49	133.08
	619.91	166.58	618.23	173.37	614.89	181.01							
	588.67	182.13	590.20	186.34	594.82	191.67							
	403.57	26.86	403.57	27.57	403.57	27.36		411.59	4.61	410.85	5.83	410.11	6.70
	212.32	−27.12	212.12	−27.54	212.12	−29.02		211.92	−31.00	212.12	−31.65	212.12	−32.35
	202.68	−22.49	202.77	−23.84	202.77	−24.62		200.81	−26.03	200.90	−26.49	201.07	−26.89
$(-1/2)$	8136.31	98.02	4602.36	102.23	2830.02	106.44	$(-1/2)$	1732.45	120.87	1719.37	121.65	1681.30	123.20
	1119.49	111.00	1114.02	114.43	1119.49	119.33		1116.75	130.76	1111.30	133.08	1119.49	133.08
	403.22	−1.31	403.22	−0.14	403.57	2.33		411.97	25.26	410.85	24.66	410.11	23.90
	212.32	−27.12	212.12	−27.54	212.12	−29.02		211.92	−31.00	212.12	−31.65	212.12	−32.35
	199.23	−21.45	199.49	−22.34	199.93	−23.35		202.77	−26.88	202.86	−27.33	202.77	−26.68
$(+3/2)$	1493.88	104.90	1493.88	107.90	1493.88	111.77	$(+3/2)$	1732.45	120.87	1719.37	121.65	1693.80	123.20
	1130.60	111.00	1125.02	114.43	1125.02	119.33		1116.75	130.76	1111.30	133.08	1119.49	133.08
	631.95	161.94	631.95	168.04	631.95	174.91		667.11	181.79	661.30	184.79		
	561.82	200.00	568.12	201.55	570.97	206.87		648.13	188.23	648.13	190.12		
	403.57	58.56	403.57	56.67	403.93	53.79		411.22	−15.08	410.48	−12.64	409.74	−9.97
	212.32	−27.12	212.12	−27.54	212.12	−29.02		211.92	−31.00	212.12	−31.65	212.12	−32.35
	205.80	−23.96	205.52	−24.96	205.24	−25.84		198.79	−25.18	199.05	−25.64	199.31	−26.13
$(-3/2)$	2149.21	101.12	2034.08	104.90	1922.50	108.68	$(-3/2)$	1474.54	123.2	1474.54	124.66	1479.33	125.43
	1119.49	111.00	1114.02	114.78	1119.49	118.56		1119.49	130.76	1111.30	133.08	1119.49	133.08
	696.69	144.50	694.56	150.52	688.27	158.16		625.87	197.77	625.87	200.00	625.01	203.44
	646.29	157.39	645.37	163.48	644.46	169.59		576.75	229.73	576.75	232.73	579.69	231.62
	403.22	−29.48	403.22	−26.38	403.22	−22.77		411.97	46.39	411.22	44.70	410.48	42.60
	212.32	−27.12	212.12	−27.54	212.12	−29.02		211.92	−31.00	212.12	−31.65	212.12	−32.35
	195.30	−19.78	196.14	−20.85	197.07	−22.13		204.41	−27.49	204.23	−28.00	204.14	−28.38
$(+5/2)$							$(+5/2)$	1451.06	123.2	1474.54	124.66	1479.33	125.43
								1119.49	130.76	1111.30	133.08	1119.49	133.08
	635.47	160.48	633.70	166.92	633.70	174.91		696.69	172.59	694.56	175.69	690.35	178.69
	534.15	224.40	539.21	227.41	544.37	231.96		644.46	189.35	643.55	192.43	644.46	193.90
	403.93	91.63	403.93	87.23	403.93	82.21		411.22	−34.28	410.11	−30.69	409.74	−26.69
	212.32	−27.12	212.12	−27.54	212.12	−29.02		211.92	−31.00	212.12	−31.65	212.12	−32.35
	208.91	−25.08	208.43	−26.06	207.96	−27.11		196.22	−24.13	196.82	−24.61	197.50	−25.31
$(-5/2)$			1238.13	111.77	1279.87	114.78	$(-5/2)$	1258.66	127.32	1276.28	127.75	1287.10	129.21
			1130.60	114.78	1125.02	119.33		1125.02	130.76	1111.30	133.08	1119.49	133.08
	795.17	129.98	759.39	138.4	743.28	146.74		631.95	195.45	632.82	196.99	628.46	200
	641.74	159.70	642.64	164.26	640.83	170.7		565.30	239.6	568.12	237.29	570.97	238.83
	402.86	−55.51	403.22	−51.23	403.22	−46.48		412.34	68.54	411.22	65.29	410.48	61.25
	212.32	−27.12	212.12	−27.54	212.12	−29.02		211.92	−31.00	212.12	−31.65	212.12	−32.35
	189.22	−17.49	190.72	−19	192.74	−20.86		206.73	−28.55	206.26	−28.84	205.89	−29.21

IV. CONCLUSIONS

A theoretical formalism of the dynamic polarizability of an atomic state due to the LG beam has been presented here in the robust form of the external field keeping in mind the trapping process of atoms or ions as the best possible application. The sum-over-states technique is used to estimate the polarizability values. The correlation exhaustive RCC theory is applied to calculate the most important and correlation-sensitive dipole matrix elements inside the sum. A list of recommended magic wavelengths in the wide range electromagnetic spectrum, from IR to UV range, is presented for $5s_{\frac{1}{2}}$ to $4d_{\frac{3}{2}}$,$4d_{\frac{5}{2}}$ transition of the Sr^+ ion. These will help to trap the atom or ion in high-precision experiments using both red- and blue-detuned techniques. Appreciable variations of magic wavelengths with the OAM, SAM, and focusing angles of the LG beam are evaluated, and they add extra freedom in the high-precision confinement approach as tunability of trapping field. For comparison, we also present our calculated magic wavelengths of the above particular transitions by using circularly and linearly polarized Gaussian beams. The new near-infrared magic wavelengths with high polarizabilities are prescribed as the best wavelengths for trapping.

ACKNOWLEDGMENT

A.B. is thankful to S. Das from Indian Institute of Technology Kharagpur for the schematic representation.

TABLE VI. Magic wavelengths (in nm) of Sr^+ for different focusing angles of the LG beam for the transitions $5s_{1/2}(+1/2) \rightarrow 4d_{5/2}(m_J)$.

	Nonparaxial LG beam											
State $[4d_{5/2}(m_J)]$	$\lambda^{50°}_{\text{magic}}$	α	$\lambda^{60°}_{\text{magic}}$	α	$\lambda^{70°}_{\text{magic}}$	α	State $[4d_{5/2}(m_J)]$	$\lambda^{50°}_{\text{magic}}$	α	$\lambda^{60°}_{\text{magic}}$	α	$\lambda^{70°}_{\text{magic}}$	α
	OAM = +2, SAM = +1							OAM = +2, SAM = −1					
(+1/2)	4423.63	98.8	2618.58	104.90	2090.06	111.00	(+1/2)	1859.73	119.76	1786.80	120.88	1732.45	123.20
	1116.75	113.23	1119.49	117.10	1125.02	123.54		1119.49	130.76	1125.02	133.08	1119.49	134.54
	619.91	169.59	616.55	177.92	614.89	188.23							
	588.67	184.02	590.96	189.35	597.94	196.99							
	403.93	27.47	404.29	27.62	404.65	26.83		411.22	4.98	410.11	6.35	408.64	7.99
	212.02	−26.57	212.12	−28.04	212.02	−30.53		212.42	−31.78	212.22	−32.35	211.92	−32.89
	202.68	−23.14	202.68	−24.09	202.86	−25.69		200.81	−26.16	200.99	−26.68	201.25	−27.25
(−1/2)	9492.37	98.02	3325.79	104.12	2373.09	110.22	(−1/2)	1732.45	121.22	1693.80	122.42	1675.12	123.88
	1116.75	113.23	1119.49	117.10	1125.02	123.54		1119.49	130.76	1125.02	133.08	1119.49	134.54
	403.57	−0.98	404.29	0.77	404.65	3.17		411.59	25.45	410.48	24.64	409.01	23.95
	212.02	−26.57	212.12	−28.04	212.02	−30.53		212.42	−31.78	212.22	−32.35	211.92	−32.89
	199.40	−21.73	199.75	−23.09	200.28	−24.60		202.86	−27.33	202.86	−27.61	202.86	−27.79
(+3/2)	1493.88	106.44	1493.88	110.22	1479.33	115.21	(+3/2)	1719.37	121.22	1693.80	122.42	1675.12	123.88
	1116.75	113.23	1119.49	117.10	1125.02	123.54		1119.49	130.76	1125.02	133.08	1119.49	134.54
	633.70	164.69	631.95	171.91	631.95	180.67		667.11	181.79	659.38	186.68		
	565.30	200.77	570.97	205.33	572.40	211.43		646.29	190.89	649.98	191.24		
	403.93	58.58	404.29	55.64	404.65	51.65		411.22	−14.05	410.11	−11.07	408.64	−7.91
	212.02	−26.57	212.12	−28.04	212.02	−30.53		212.42	−31.78	212.22	−32.35	211.92	−32.89
	205.70	−24.37	205.33	−25.48	205.06	−26.51		198.88	−25.41	199.23	−25.75	199.58	−26.41
(−3/2)	2090.06	101.8	1963.94	107.13	1844.67	112.46	(−3/2)	1474.54	123.2	1474.54	125.09	1479.33	125.86
	1116.75	113.23	1119.49	117.10	1125.02	123.54		1119.49	130.76	1125.02	133.08	1119.49	134.54
	696.69	147.51	692.45	154.73	682.09	163.49		626.73	198.54	626.73	201.55	626.73	204.64
	642.64	160.48	644.46	167.27	647.21	175.26		575.29	231.27	579.69	232.73	579.69	233.51
	403.57	−28.85	403.93	−24.91	404.29	−20.66		411.59	45.92	410.48	43.73	409.01	40.98
	212.02	−26.57	212.12	−28.04	212.02	−30.53		212.42	−31.78	212.22	−32.35	211.92	−32.89
	195.72	−20.32	196.48	−21.86	197.76	−23.53		204.41	−27.71	204.23	−28.06	204.05	−28.63
(+5/2)					1171.29	120.10	(+5/2)	1451.06	123.2	1474.54	125.09	1479.33	125.86
					1144.81	121.99		1119.49	130.76	1125.02	133.08	1119.49	134.54
	633.70	162.71	631.95	171.91	633.70	180.24		696.69	174.14	692.45	177.23	686.20	181.36
	536.67	225.17	541.78	230.50	548.30	233.51		642.64	191.24	646.29	193.21	646.29	194.67
	404.29	90.32	404.29	84.88	404.65	78.14		410.85	−32.86	409.74	−28.91	408.27	−23.69
	212.02	−26.57	212.12	−28.04	212.02	−30.53		212.42	−31.78	212.22	−32.35	211.92	−32.89
	208.72	−25.58	208.15	−26.59	207.58	−27.87		196.39	−24.24	197.07	−25.06	198.02	−25.60
(−5/2)	1180.40	110.65	1269.17	114	1340.10	118.21	(−5/2)	1262.14	126.98	1283.47	128.52	1287.10	129.98
	1130.60	112.45	1119.49	117.10	1125.02	123.54		1119.49	130.76	1125.02	133.08	1119.49	134.54
	781.53	132.3	753.11	143.3	729.01	153.61		631.95	195.45	632.82	199.23	631.07	201.55
	640.83	161.94	640.83	168.81	642.64	176.03		568.12	239.6	569.54	238.4	572.40	240.38
	403.57	−54.76	403.93	−49.37	404.29	−42.34		411.97	67.26	410.48	63.32	409.37	58.69
	212.02	−26.57	212.12	−28.04	212.02	−30.53		212.42	−31.78	212.22	−32.35	211.92	−32.89
	189.61	−18.1	191.68	−19.65	194.05	−21.88		206.54	−28.87	206.17	−29.07	205.70	−29.17

[1] C. Champenois, M. Houssin, C. Lisowski, M. Knoop, G. Hagel, M. Vedel, and F. Vedel, Phys. Lett. A **331**, 298 (2004).

[2] C. W. Chou, D. B. Hume, J. C. J. Koelemeij, D. J. Wineland, and T. Rosenband, Phys. Rev. Lett. **104**, 070802 (2010).

[3] H. S. Margolis, J. Phys. B: At., Mol. Opt. Phys. **42**, 154017 (2009).

[4] V. D. Ovsiannikov, V. G. Pal'chikov, A. V. Taichenachev, V. I. Yudin, H. Katori, and M. Takamoto, Phys. Rev. A **75**, 020501(R) (2007).

[5] J. McKeever, J. R. Buck, A. D. Boozer, A. Kuzmich, H.-C. Nagerl, D. M. Stamper-Kurn, and H. J. Kimble, Phys. Rev. Lett. **90**, 133602 (2003).

[6] S. Stellmer, M. K. Tey, B. Huang, R. Grimm, and F. Schreck, Phys. Rev. Lett. **103**, 200401 (2009).

[7] X. Xu, T. H. Loftus, J. L. Hall, A. Gallagher, and J. Ye, J. Opt. Soc. Am. B **20**, 968 (2003).

[8] T. Nicholson, S. Campbell, R. Hutson, G. Marti, B. Bloom, R. McNally, W. Zhang, M. Barrett, M. Safronova, G. Strouse *et al.*, Nat. Commun. **6**, 6896 (2015).

[9] B. Arora, M. S. Safronova, and C. W. Clark, Phys. Rev. A **76**, 052509 (2007).

[10] A. D. Ludlow *et al.*, Science **319**, 1805 (2008).

[11] V. V. Flambaum, V. A. Dzuba, and A. Derevianko, Phys. Rev. Lett. **101**, 220801 (2008).

[12] B. Arora and B. K. Sahoo, Phys. Rev. A **86**, 033416 (2012).
[13] T. Kuga, Y. Torii, N. Shiokawa, T. Hirano, Y. Shimizu, and H. Sasada, Phys. Rev. Lett. **78**, 4713 (1997).
[14] T. Otsu, T. Ando, Y. Takiguchi, Y. Ohtake, H. Toyoda, and H. Itoh, Sci. Rep. **4**, 4579 (2014).
[15] A. D. Kiselev and D. O. Plutenko, Phys. Rev. A **94**, 013804 (2016).
[16] S. A. Kennedy, G. W. Biedermann, J. T. Farrar, T. G. Akin, S. P. Krzyzewski, and E. R. I. Abraham, Opt. Commun. **321**, 110 (2014).
[17] L. Allen, M. W. Beijersbergen, R. J. C. Spreeuw, and J. P. Woerdman, Phys. Rev. A **45**, 8185 (1992).
[18] P. K. Mondal, B. Deb, and S. Majumder, Phys. Rev. A **89**, 063418 (2014).
[19] A. Bhowmik, P. K. Mondal, S. Majumder, and B. Deb, Phys. Rev. A **93**, 063852 (2016).
[20] C. T. Schmiegelow, J. Schulz, H. Kaufmann, T. Ruster, U. G. Poschinger, and F. Schmidt-Kaler, Nat. Commun. **7**, 12998 (2016).
[21] P. B. Monteiro, P. A. M. Neto, and H. M. Nussenzveig, Phys. Rev. A **79**, 033830 (2009).
[22] L. Marrucci, C. Manzo, and D. Paparo, Phys. Rev. Lett. **96**, 163905 (2006).
[23] Y. Zhao, J. S. Edgar, G. D. M. Jeffries, D. McGloin, and D. T. Chiu, Phys. Rev. Lett. **99**, 073901 (2007).
[24] J. Mitroy, M. S. Safronova, and C. W. Clark, J. Phys. B: At., Mol. Opt. Phys. **43**, 202001 (2010).
[25] M. S. Safronova and U. I. Safronova, Phys. Rev. A **83**, 012503 (2011).
[26] T. K. Ghosh, A. K. Das, M. Castro, S. Canuto, and P. K. Mukherjee, Phys. Rev. A **48**, 2686 (1993).
[27] N. N. Dutta, S. Roy, and P. C. Deshmukh, Phys. Rev. A **92**, 052510 (2015).
[28] B. Richards and E. Wolf, Proc. R. Soc. London, Ser. A **253**, 358 (1959).
[29] A. Boivin and E. Wolf, Phys. Rev. **138**, B1561 (1965).
[30] K. Raghavachari, G. W. Trucks, J. A. Pople, and M. Head-Gordon, Chem. Phys. Lett. **157**, 479 (1989).
[31] N. N. Dutta, S. Roy, G. Dixit, and S. Majumder, Phys. Rev. A **87**, 012501 (2013).
[32] N. N. Dutta and S. Majumder, Indian J. Phys. **90**, 373 (2016).
[33] S. Roy, N. N. Dutta, and S. Majumder, Phys. Rev. A **89**, 042511 (2014).
[34] A. Bhowmik, S. Roy, N. N. Dutta, and S. Majumder, J. Phys. B: At., Mol. Opt. Phys. **50**, 125005 (2017).
[35] A. Bhowmik, N. N. Dutta, and S. Roy, Astrophys. J. Lett. **836**, 125 (2017).
[36] A. Das, A. Bhowmik, N. N. Dutta, and S. Majumder, J. Phys. B: At., Mol. Opt. Phys. **51**, 025001 (2018).
[37] U. I. Safronova, Phys. Rev. A **82**, 022504 (2010).
[38] E. H. Pinnington, R. W. Berends, and M. Lumsden, J. Phys. B: At., Mol. Opt. Phys. **28**, 2095 (1995).
[39] A. Gallagher, Phys. Rev. **157**, 24 (1967).
[40] A. Kramida, Yu. Ralchenko, J. Reader, and NIST ASD Team. NIST Atomic Spectra Database (ver. 5.1), http://physics.nist.gov/asd
[41] W. R. Johnson, Z. W. Liu, and J. Sapirstein, At. Data Nucl. Data Tables **64**, 279 (1996).
[42] J. Kaur, S. Singh, B. Arora, and B. K. Sahoo, Phys. Rev. A **92**, 031402(R) (2015).
[43] D. Jiang, B. Arora, M. S. Safronova, and C. W. Clark, J. Phys. B: At., Mol. Opt. Phys. **42**, 154020 (2009).
[44] P. S. Barklem and B. J. O'Mara, Mon. Not. R. Astron. Soc. **311**, 535 (2000).
[45] J. Arlt, K. Dholakia, J. Soneson, and E. M. Wright, Phys. Rev. A **63**, 063602 (2001).
[46] E. M. Wright, J. Arlt, and K. Dholakia, Phys. Rev. A **63**, 013608 (2000).